Desalination and Water Treatment
www.deswater.com
doi: 10.5004/dwt.2023.29704

299 (2023) 1–12
July

A comprehensive numerical investigation of the performance of solar stills with various designs

Vo Long Hai[a,b], Nguyen Duc Nam[b], Nguyen Minh Phu[a,*]

[a]*Faculty of Heat and Refrigeration Engineering, Industrial University of Ho Chi Minh City (IUH), Ho Chi Minh City 700000, Vietnam, Tel.: +84-906929498; email: nguyenminhphu@iuh.edu.vn (N.M. Phu), Tel.: +84-908355522; email: volonghai@iuh.edu.vn (V.L. Hai)*
[b]*Faculty of Mechanical Engineering, Industrial University of Ho Chi Minh City (IUH), Ho Chi Minh City 700000, Vietnam, Tel.: +84-937125588; email: nguyenducnam@iuh.edu.vn (N.D. Nam)*

Received 19 March 2023; Accepted 15 June 2023

ABSTRACT

Passive solar distillers are widely used due to their portability and simplicity. Passive solar stills have various designs. However, no study in the literature has compared them according to the laws of thermodynamics. In this paper, five passive solar stills were investigated numerically to evaluate their water productivity and entropy generation. Laminar flow and a 2D computational domain of humid air in still enclosures were simulated using the species transport model. The solar stills included two double-slope solar stills (DSS1 and DSS2), a single-slope still (SSS), a tubular solar still (TuSS), and a triangle solar still (TrSS). All of the stills had an identical water surface length of 102 mm. The effects of the water surface temperature, which ranged from 50°C to 80°C, on convection heat transfer, freshwater production, and entropy generation were investigated. The simulation results showed that the TuSS obtained the highest water production and the smallest total entropy generation. At high operating temperatures, the productivity of the TuSS was nearly two times that of the SSS. Two recirculating zones were observed inside the distillation enclosures, except for the SSS. When the water temperature was greater or lower than 53°C, one recirculating zone and three recirculating zones were created in the SSS, respectively. The change in the number of vortices caused distinct transport characteristics in the SSS. An impinging jet on the water surface in the DSS2 led to the largest entropy generation among the examined stills. Large dead zones on the water surface of the DSS1 caused a reduction in evaporation. Therefore, the TuSS and TrSS designs eliminated the zones due to clearances between the water surface and glass cover.

Keywords: Passive solar still; Species transport model; Diffusive irreversibility; Circulation formation; Natural convection

1. Introduction

Drinking water is essential for humans, plants, and animals; however, 97% of Earth's water is located in oceans, 2% is stored in the form of ice in the Arctic and Antarctic regions, and only 1% constitutes fresh water [1]. In countries with long coastlines and many islands, such as Vietnam, portable water is not only extremely necessary but also scarce. Therefore, freshwater production technologies and equipment productivity improvements are in place. The simplest way to produce fresh water is to evaporate impure water and condense the steam into freshwater. However, this method consumes large amounts of energy because of the great latent heat production during the water vaporization [2]. Waste heat and renewable energy, such as solar energy, are feasible heat sources to perform this type of distillation. Solar distillation is classified into active and passive types. The active type is more productive due to its additional auxiliary solar collector and recirculating pump. However, the passive type is simple to manufacture and operate,

* Corresponding author.

making it suitable for use in remote and inaccessible areas [3]. There are various configurations of passive solar stills, such as the single-slope type, double-slope type, tubular type [4], etc. Double-slope stills are generally divided into the following two types: V-type stills and greenhouse-type stills [5]. V-type stills are less studied, specifically their flow field and the diffusion of the air–water vapor mixture in their distillation chambers. However, a few analytical and experimental studies exist [6,7].

Computational fluid dynamics (CFD) studies are often used due to their efficient numerical simulations, and transport phenomena in the distillation chambers of stills can be explained visually [8–10]. Keshtkar et al. [11] numerically investigated single-slope and multi-stage double-slope solar stills. One vortex was observed inside the single-slope still. The number of vortices in the double-slope solar still increased with the decrease in the operating temperature. Six vortices were found when the operating temperature was not high enough. Additionally, Keshtkar et al. [12] compared the performances of single-slope and stepped solar stills. They reported that the water production of the stepped solar still was 17.4% higher than that of the single-slope solar still. Ashtiani and Hormozi [13] optimized the design of a stepped solar still in terms of entropy generation minimization. Their results showed that the irreversibility of the stepped still increased with the step height. Rahbar and Esfahani [14] simulated the operation of a single-slope still using CFD and the Chilton–Colburn analogy. They concluded that there was a good match between the CFD predictions and the Chilton–Colburn model. In addition, two recirculating zones appeared in the still. Shoeibi et al. [15] numerically considered a double-slope solar still with two types of glass cooling, that is, water cooling and nanofluid cooling. Three vortices were discovered in the distillation chamber of the still at all times of the day. Additionally, optimal nanofluid concentrations and performance improvements were analyzed. Edalatpour et al. [16] positioned a partition wall in a single-slope solar still, which changed the flow field to four recirculating zones. The positive and negative impacts of the wall position on water production were analyzed. Rashidi et al. [17] compared the performances of traditional and nanofluid single-slope solar stills. They concluded that water productivity increased with the increase in nanofluid concentration. The stills created three vortices that enhanced heat and mass transfer.

In recent years, tubular solar stills have received attention from scholars due to their efficiency improvements; additionally, their water basins are placed inside their tubular glass covers, which results in minimal heat loss [18,19]. Rahbar et al. [10] simulated and compared the performance and entropy generation of tubular and triangular solar stills. The tubular still obtained the highest water production and the lowest entropy generation due to the larger vortex that formed. Subhani and Kumar [20] investigated a tubular still with a curved basin and compared it with a single-slope solar still. The modified basin showed better thermal dissipation due to its smaller displacement area. Yan et al. [21] evaluated a tubular solar still under vacuum operating conditions. They confirmed that freshwater production was sharply enhanced due to an increase in mass diffusivity at low pressures. Additionally, the flow pattern was affected by the operating pressure and water depth.

A literature review implied that there have been numerous attempts to compare the performances of two solar stills. However, comprehensive comparisons across more categories were not found. In addition, up to date, transport phenomena or entropy generation analyses of V-type solar stills have not been reported. Furthermore, there were discrepancies in the flow field of the single-slope solar still studied. In this paper, five passive solar stills were simulated simultaneously in order to investigate their flow fields, water production, and entropy generation.

2. Model description

2.1. Computational domains

A total of 5 computational domains corresponding to 5 passive solar stills, including a double-slope solar still with condensation traps placed at its vertical walls (DSS1), a solar still with a condensation trap placed in the middle of its glass covers (DSS2), a single-slope still (SSS), a tubular solar still (TuSS), and a triangular solar still (TrSS), are shown in Fig. 1. All of the stills had an identical water surface value of L = 102 mm. Other dimensions are also shown in the figure. It should be noted that the DSS2 (V-type still) is usually rare to find in the literature. In a still, solar radiation shines through the glass cover to the water basin, which causes the water to receive heat and evaporate at the water surface. Therefore, the fluid in the computational domain was humid air, and the water and glass cover surfaces were assumed to be saturated humid air (j = 100%).

2.2. Mathematical formulation

The natural convection of the air–water vapor mixture in the two-dimensional domain with steady and laminar flow assumptions was expressed using the following governing equations [10,14,15]:

The continuity equation:

$$\frac{\partial u}{\partial x}+\frac{\partial v}{\partial y}=0 \tag{1}$$

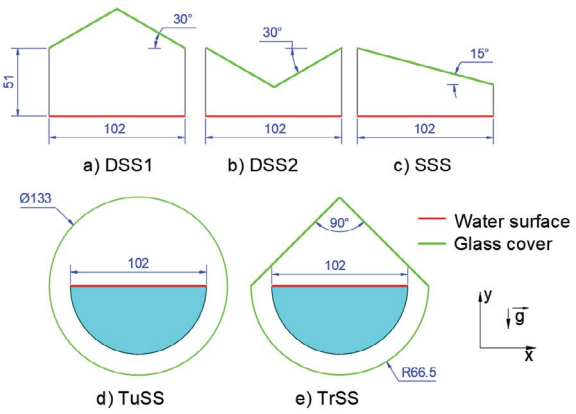

Fig. 1. Five passive solar stills investigated in this study (dimensions in millimeters). (a) DSS1, (b) DSS2, (c) SSS, (d) TuSS and (e) TrSS.

The x-momentum equation:

$$u\frac{\partial u}{\partial x}+v\frac{\partial u}{\partial y}=-\frac{1}{\rho}\frac{\partial p}{\partial x}+\nu\left(\frac{\partial^2 u}{\partial x^2}+\frac{\partial^2 u}{\partial y^2}\right) \tag{2}$$

The y-momentum equation:

$$u\frac{\partial v}{\partial x}+v\frac{\partial v}{\partial y}=-\frac{1}{\rho}\frac{\partial p}{\partial y}+\nu\left(\frac{\partial^2 v}{\partial x^2}+\frac{\partial^2 v}{\partial y^2}\right)+g\beta\left(T-T_o\right)+g\beta_s\rho\left(Y-Y_o\right) \tag{3}$$

The energy equation:

$$u\frac{\partial T}{\partial x}+v\frac{\partial T}{\partial y}=\alpha\left(\frac{\partial^2 T}{\partial x^2}+\frac{\partial^2 T}{\partial y^2}\right) \tag{4}$$

The water vapor mass fraction equation [22]:

$$u\frac{\partial Y}{\partial x}+v\frac{\partial Y}{\partial y}=D_m\left(\frac{\partial^2 Y}{\partial x^2}+\frac{\partial^2 Y}{\partial y^2}\right) \tag{5}$$

The mass diffusivity of vapor in the air (D_m) was calculated as follows [11,23]:

$$D_m=2.6\times10^{-5}\left(\frac{101325}{p}\right)\left(\frac{T}{298}\right)^{1.5} \tag{6}$$

The boundary conditions associated with partial differential Eqs. (1)–(5) were applied as follows:

- At the water surface: $u = v = 0$, $T = T_w$, $Y=Y\big|_{T=T_w,\varphi=100\%}$,
- At the glass cover: $u = v = 0$, $T = T_g$, $Y=Y\big|_{T=T_g,\varphi=100\%}$,
- Other walls: $u = v = 0$, $\frac{\partial T}{\partial n}=0,\frac{\partial Y}{\partial n}=0$.

From the simulated temperature and vapor mass fraction fields, the convective heat transfer coefficient (h_c) between the glass cover and the water surface and the hourly water yield ($\dot{m}$) were estimated as follows [10,11]:

$$h_c=\frac{-k}{L\left(T_w-T_g\right)}\int_o^L\left.\frac{\partial T}{\partial y}\right|_{\text{water surface}}dx \tag{7}$$

$$\dot{m}=\frac{-3600D_m\rho}{L}\int_o^L\left.\frac{\partial Y}{\partial y}\right|_{\text{water surface}}dx \tag{8}$$

Entropy generation, or irreversibility, represents useful work destruction mechanisms. Therefore, water productivity was manifested via entropy generation. The local volumetric entropy generation inside the stills was evaluated after the temperature, velocity, and mass fraction distributions were determined. The local volumetric entropy generations contained friction ($S_{\text{gen},f}$), heat transfer ($S_{\text{gen},t}$), and mass transfer ($S_{\text{gen},m}$) calculations, expressed as follows [10,24,25]:

$$S_{\text{gen},f}=\frac{\mu}{T}\left\{2\left[\left(\frac{\partial u}{\partial x}\right)^2+\left(\frac{\partial v}{\partial y}\right)^2\right]+\left(\frac{\partial u}{\partial y}+\frac{\partial v}{\partial x}\right)^2\right\} \tag{9}$$

$$S_{\text{gen,t}}=\frac{k}{T^2}\left[\left(\frac{\partial T}{\partial x}\right)^2+\left(\frac{\partial T}{\partial y}\right)^2\right] \tag{10}$$

$$S_{\text{gen},m}=\frac{\text{RD}_m\rho}{Y}\left[\left(\frac{\partial Y}{\partial x}\right)^2+\left(\frac{\partial Y}{\partial y}\right)^2\right]+\frac{\text{RD}_m\rho}{T}\left[\frac{\partial T}{\partial x}\frac{\partial Y}{\partial x}+\frac{\partial T}{\partial y}\frac{\partial Y}{\partial y}\right] \tag{11}$$

The total entropy generation was represented by the sum of the entropy generation components as follows:

$$S_{\text{gen,total}}=S_{\text{gen},f}+S_{\text{gen},t}+S_{\text{gen},m} \tag{12}$$

2.3. Numerical methodology

The numerical solutions of the solar stills were carried out in the ANSYS Fluent 19.2 software under atmospheric conditions. A 2D quadrilateral mesh with highly refined density near the glass cover and water surfaces was employed, as illustrated in Fig. 2. A grid independence test was performed for a typical case with various mesh sizes, as shown in Table 1. The deviation in hourly productivity of the 76,280 mesh elements was negligible, which revealed that grid independence was obtained. Therefore, the mesh size of 76,280 elements was selected for further consideration to ensure numerical accuracy and computational cost.

The mass diffusion coefficient in Eq. (6) was interpreted by a user-defined function (UDF) in the Fluent software.

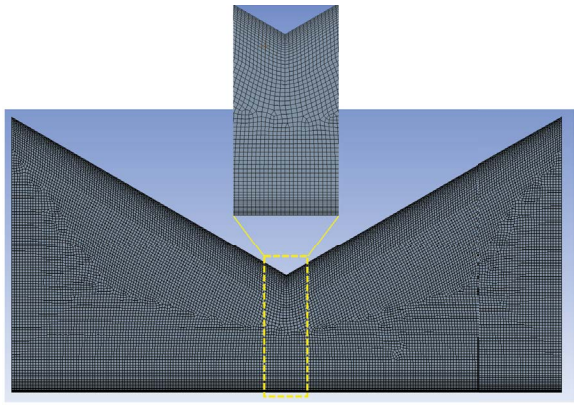

Fig. 2. Numerical simulation of the representative implemented grid.

Table 1
Study of grid independence

Mesh elements	Hourly yield (kg/m²·h)	Deviation (%)
18257	0.756582	–
25385	0.786188	3.91
39039	0.794286	1.03
52021	0.809148	1.87
76280	0.814432	0.65
130055	0.807652	0.83

The entropy generations were defined as custom-field functions in the software. The convection heat transfer coefficient and hourly yield rate equations were composed using expressions in the CFD-Post software. The species transport model was activated for the air–water vapor mixture. Incompressible ideal gas was referred to by density, mixing law by specific heat capacity, mass-weighted mixing law by thermal conductivity and viscosity, and kinetic theory by thermal diffusion coefficient [21].

Double-precision and pressure-based solvers were adopted for the governing equations. The pressure–velocity coupling was treated by using the SIMPLE (semi-implicit method for pressure-linked equations) algorithm. A second-order upwind scheme was used to discretize a convection term, whereas the PRESTO! (PREssure STaggering Option) scheme was employed for pressure interpolation [11]. A residual of 10^{-6} was set for the energy equation and 10^{-3} for the others. To ensure convergence in all cases, the under-relaxation factors of the pressure and momentum equations were reduced. In this study, a factor of 0.1 for the pressure and a value of 0.3 for the momentum were assigned.

2.4. Model validation

Before the start of the investigation, a model validation was conducted. The convection heat transfer coefficient, which was computed using Eq. (7), was compared with the most well-known correlation of Dunkle for the single-slope still (SSS). Fig. 3 represents the coefficient and the water surface temperature (T_w), whereas the temperature difference between the water surface and the glass cover ($T_w - T_g$) was fixed at 10 K. The numerical simulation results in this study were closely matched with those of the correlation. The current results were negligibly underestimated. A maximum error of 3.2% was acceptable for further examination. Dunkle's correlation is expressed as follows [14,18]:

$$h_c = 0.884\left[T_w - T_g + \left(p_w - p_g\right)\frac{T_w + 273}{268.9\times10^3 - p_w}\right]^{1/3} \tag{13}$$

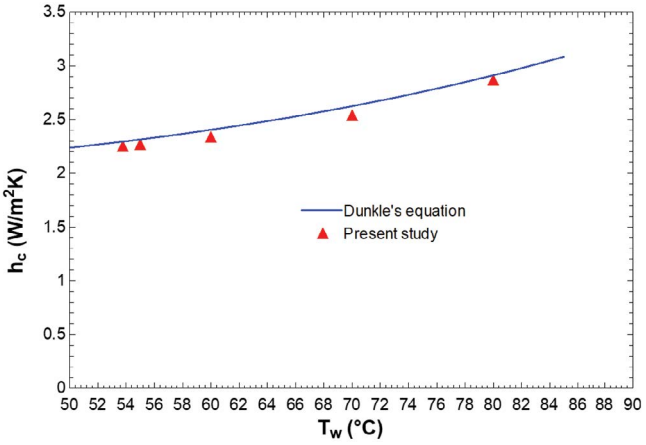

Fig. 3. Comparison of the convective heat transfer coefficient h_c for the single-slope still (SSS).

where p_w and p_g are the partial pressures of the vapor at water surface and glass cover temperatures, respectively.

3. Results and discussion

The effects of the water surface temperature, which ranged from 50°C to 80°C, on the performances of the five solar stills are presented in this section. The temperature difference between the glass cover and the water surface was fixed at 10 K. Figs. 4–10 display the thermohydraulic and entropy generation distributions at a water surface temperature of 60°C. The water vapor mass fraction and temperature fields are presented in Figs. 4 and 5. The mass fractions of the DSS1, TuSS, and TrSS cases were almost identical, that is, a higher mass fraction concentrated in the middle of the water surface. The DDS2 and SSS cases were grouped together because the DSS2 nearly consists of two single-slope stills located symmetrically. The temperature and vapor mass fraction variations in the stills were almost uniform.

Despite the identical passive solar still type and water surface dimensions, the flow patterns of the stills changed significantly, as shown in Fig. 6. These phenomena resulted in the stills' different transport behaviors. High-speed natural convection streams moved upwards at the centers of the DSS1, TuSS, and TrSS. This flow pattern created two primary vortices, which included a counterclockwise vortex on the left-hand side and a clockwise vortex on the right-hand side. For DSS2, the direction of the two primary vortices was reversed. Furthermore, there was an impinging jet acting on the water surface that prevented water evaporation (Fig. 6b). For SSS, there was only one primary vortex. The general trend was that the air–vapor mixture followed the condensation surface in a top-to-bottom direction; thus, two vortices were created for the symmetric stills (DSS1, DSS2, TuSS, and TrSS), and one vortex was formed in the SSS. The fluid velocities in the DSS1 and TuSS were at their maximum, followed by the TrSS, SSS, and DSS2. The number of vortices and the natural convection velocity's impact on heat and mass transfers resulted in enhanced water productivity. Moreover, the strength of the recirculation zone in the TuSS was greater than that of the DSS2 and TrSS, which may have led to higher potable water production in the TuSS. Large dead zones in the lower corners were observed for the DSS1. These zones reduced water evaporation and produced higher temperatures at the corners of DSS1, as shown in Figs. 4 and 5. The clearances on either side of the water surface with the glass cover in the TuSS and TrSS diminished their dead vortex zones. Hence, the water vapor moved upwards with a greater water surface area compared to DSS1. Fig. 7 presents the change in u-velocity in the y-direction at the water surface's left half in the TuSS, TrSS, and DSS1. The velocity gradients of the TuSS and TrSS showed positive values, which indicated irrotational flow on the water surface. Flow separation (du/dy = 0) was found on the water surface of DSS1 at x = 16 mm. A strong secondary vortex (du/dy < 0) of DSS1 caused a reduced evaporation surface.

The local volumetric entropy generation is presented in Figs. 8–11. The frictional entropy generation was very small due to the low speed of natural convection currents.

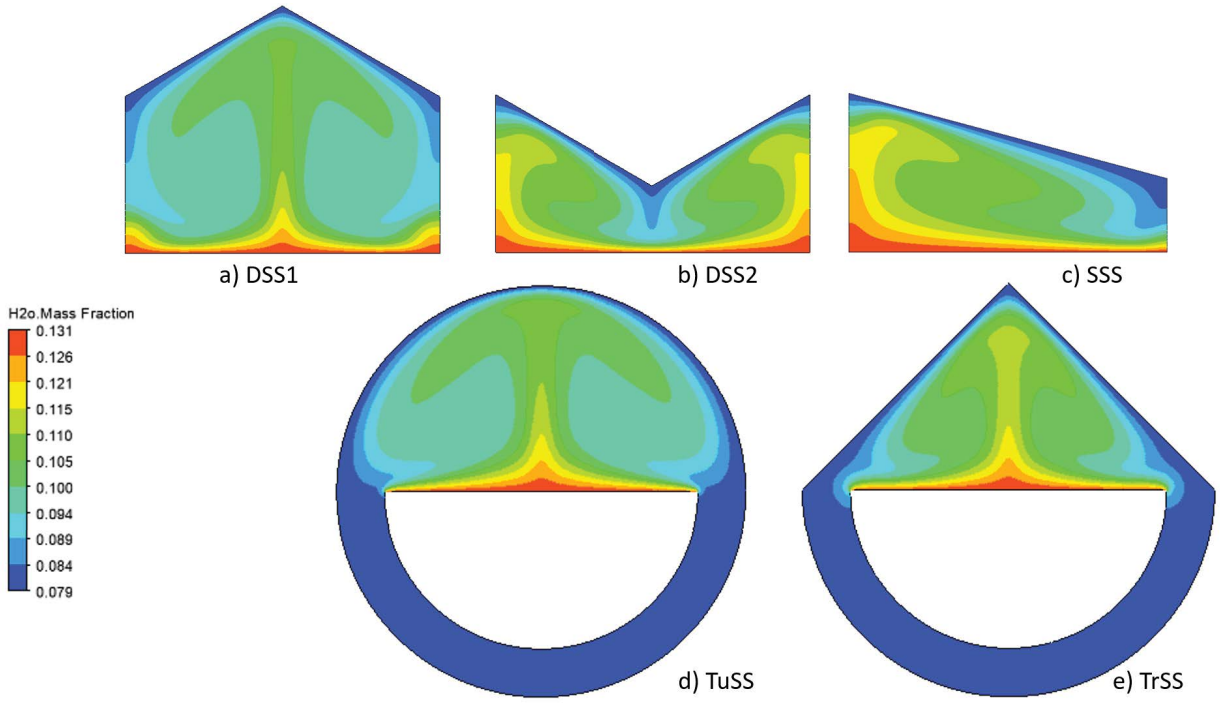

Fig. 4. Water vapor distribution inside the solar stills at T_w = 60°C. (a) DSS1, (b) DSS2, (c) SSS, (d) TuSS and (e) TrSS.

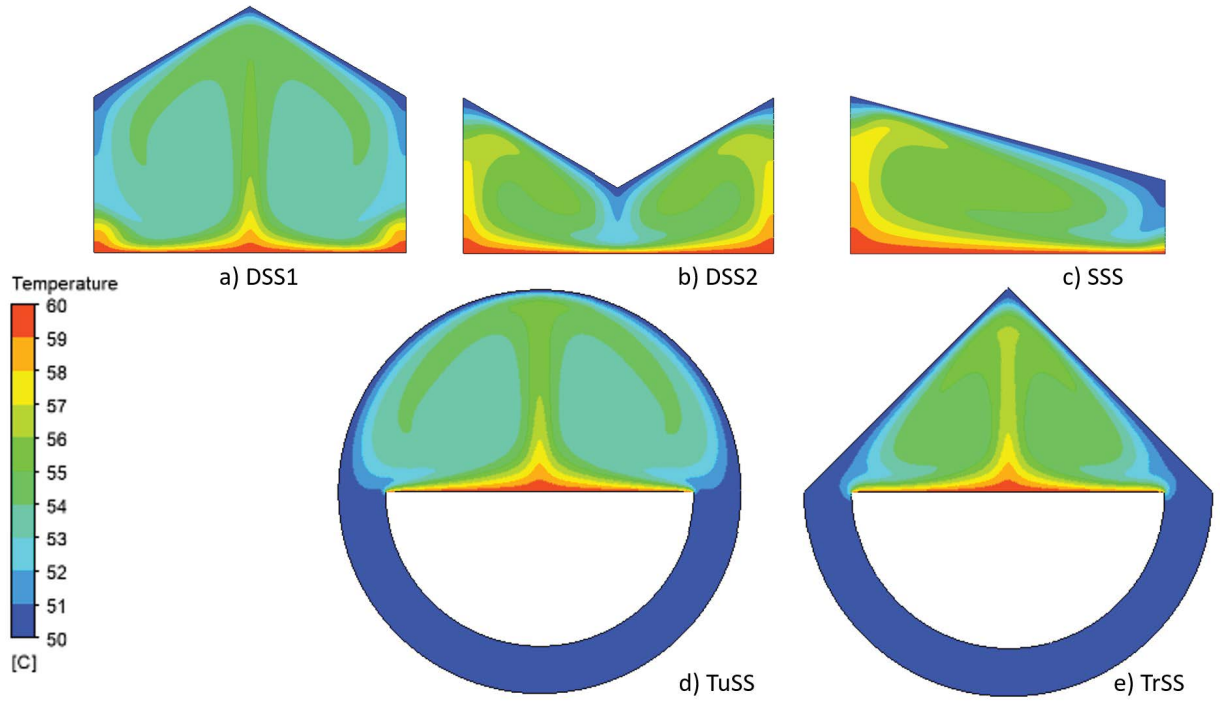

Fig. 5. Contour of isotherms inside the solar stills at T_w = 60°C. (a) DSS1, (b) DSS2, (c) SSS, (d) TuSS and (e) TrSS.

Locations that generate large frictional entropy were found near the surfaces, as shown in Fig. 8. These locations experienced large friction between the fluid flow and stationary walls.

The greatest entropy generation caused by heat and mass transfer in the SSS occurred at reattachment points on the glass cover and water surface (Figs. 9c and 10c). A large entropy generation caused by heat and mass transfer in the TuSS occurred at the peak of the glass cover (Figs. 9d and 10d). The largest entropy generation due to heat and mass transfer in the DSS2 happened at the stagnation point on the water surface (Figs. 9b and 10b). This was caused by the

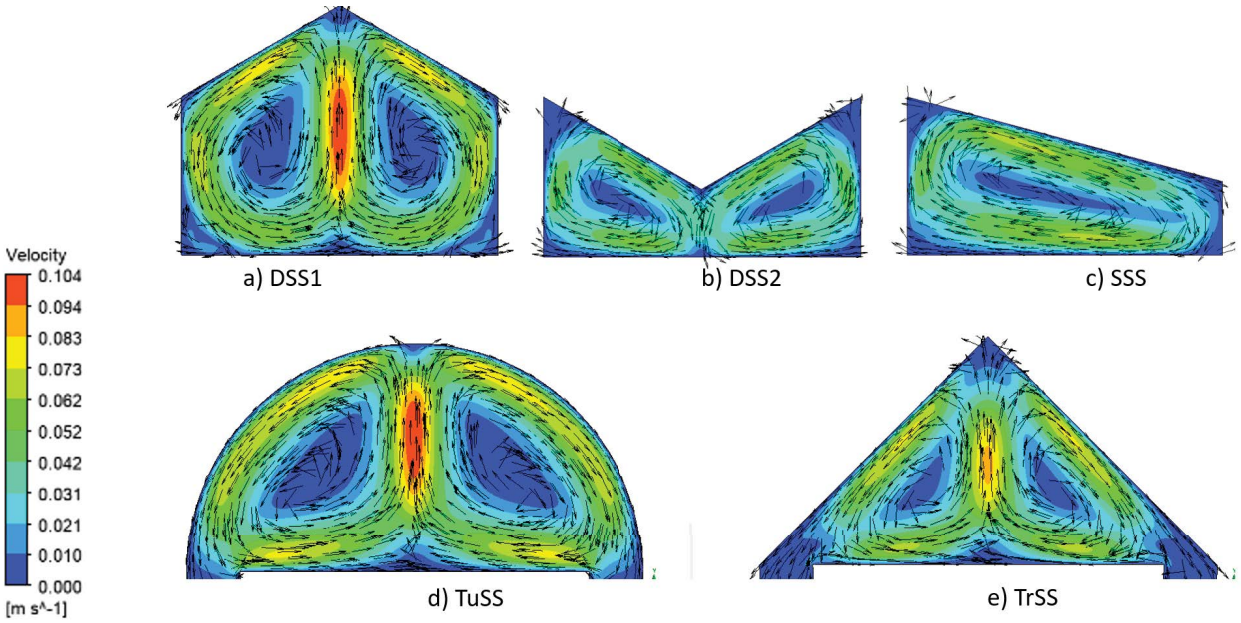

Fig. 6. Velocity vector and velocity magnitude inside the solar stills at T_w = 60°C. (a) DSS1, (b) DSS2, (c) SSS, (d) TuSS and (e) TrSS.

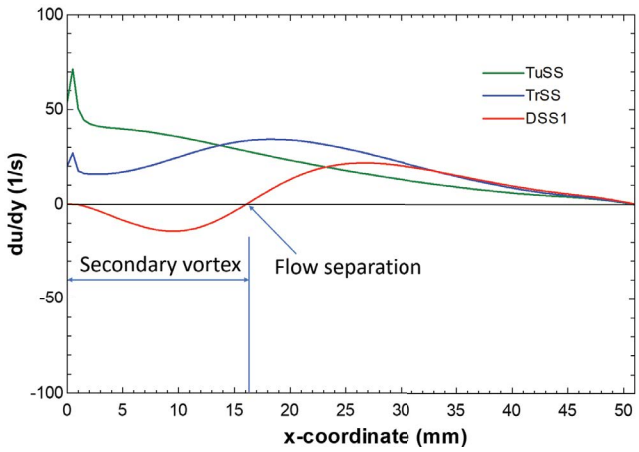

Fig. 7. Velocity gradient at half the water surface (x = 0 to L/2).

above-mentioned impinging jet analysis. A very large irreversibility on the left and right sides of the water surfaces in the TuSS and TrSS is shown in Figs. 9d, 9e, 10d, and 10e. The upward flow made contact with the downward flow at these locations, causing sharp differences in the temperature and water vapor concentrations. Among the three types of entropy generation, entropy generation caused by mass transfer had the largest value, which proved that mass transportation was dominant over other transport mechanisms in distillation enclosures. Thus, the distributions of total entropy generation and entropy generation caused by mass transfer were almost uniform, as shown in Figs. 10 and 11.

The convection heat transfer coefficient between the water surface and the cover glass, along with the water temperature for the stills, is shown in Fig. 12. The water surface temperature varied in the range of 50°C–80°C, with increments of 10°C. The general trend was that as the temperature increased, the coefficient increased because the velocity of a mixture in an enclosure would increase. The coefficient of TuSS was the largest, followed by TrSS. The convection heat transfer coefficient of SSS was the smallest, except at water temperatures less than 53.8°C. Fig. 6 shows the velocity distributions in the stills based on the above comments. The TuSS and TrSS had strong buoyancy forces. The mixture velocity of DSS1 was also high, but a large dead vortex existed on either side of the water surface. The SSS had a low convection heat transfer coefficient because there was only one primary vortex (as illustrated in Fig. 6c). The simulation results showed that the convection heat transfer coefficient of SSS increased when T_w = 50°C. Hence, the simulation of the SSS was extended to the following temperatures: T_w = 51.8°C, 52.5°C, 53.1°C, 53.8°C, and 55°C. At water temperatures less than 53.8°C, the heat transfer coefficient of SSS was higher than that of DSS1 and DSS2. In addition, the convection heat transfer coefficient of SSS at water temperatures less than 53.8°C was roughly equal to that at 80°C.

The velocity vector of SSS was investigated based on different water temperatures, as shown in Fig. 13. At the low temperature of 50°C, three primary vortices appeared in the SSS enclosure. The number of vortices increased from one to three when the water surface temperature decreased from 60°C to 50°C, which intensified the convection heat transfer coefficient even though the convection velocity decreased with the decrease in temperature. Therefore, using the information from Fig. 12, it was possible to allocate the water temperature of 53°C as the critical temperature for the transition from one vortex to three vortices in the single-slope still (SSS). The increase in the number of vortices at low operating temperatures can be explained by the low mixture velocity, which resulted in insufficient driving force along the water surface and the glass cover. Therefore, flow separation occurred, leading to an increase in the number of vortices.

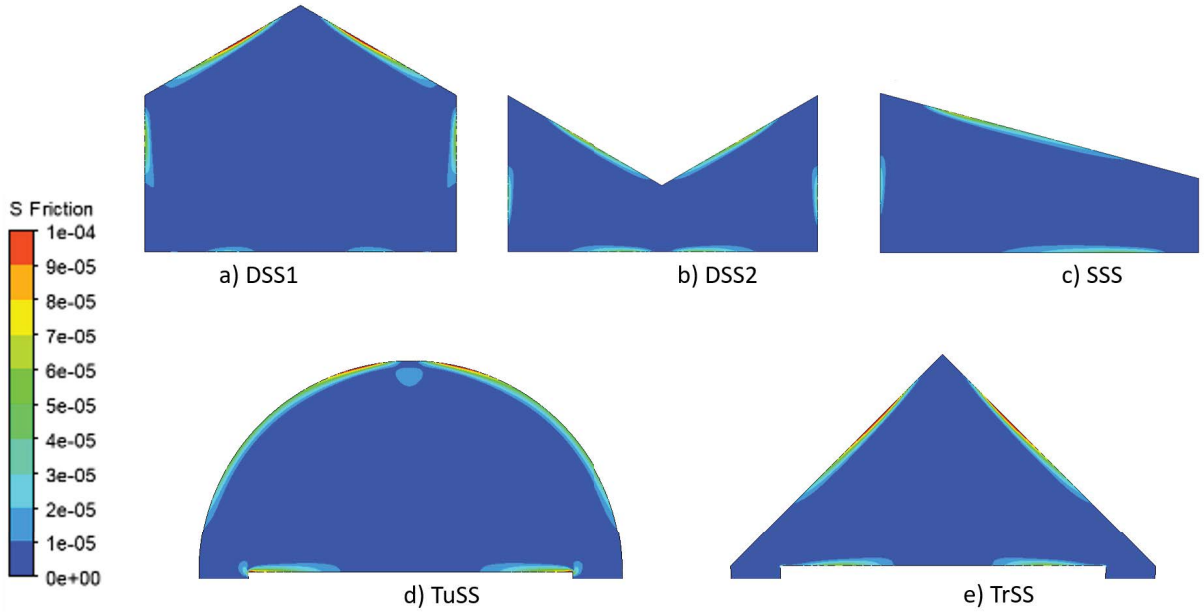

Fig. 8. Entropy generation caused by friction (W/m³·K) inside the solar stills at T_w = 60°C. (a) DSS1, (b) DSS2, (c) SSS, (d) TuSS and (e) TrSS.

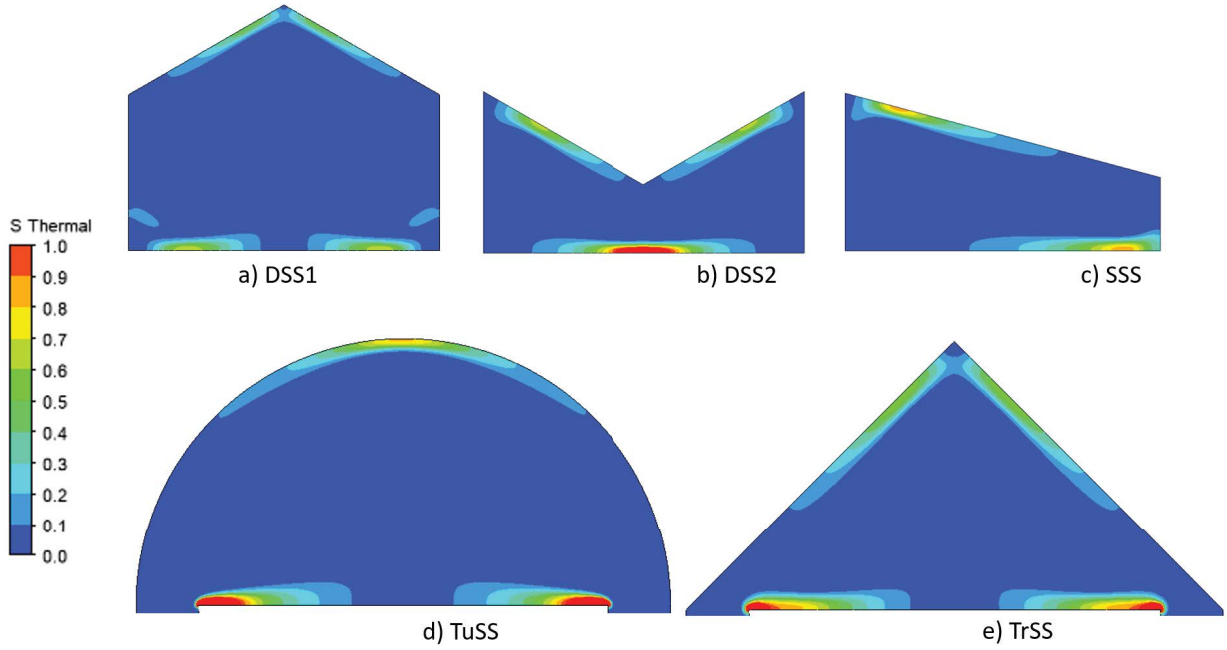

Fig. 9. Entropy generation caused by heat transfer (W/m³·K) inside the solar stills at T_w = 60°C. (a) DSS1, (b) DSS2, (c) SSS, (d) TuSS and (e) TrSS.

The water production trend is identical to that of the convection heat transfer coefficient, as shown in Fig. 14. The water production by TuSS was the largest, followed by TrSS. The productivity of SSS was the smallest, except at water temperatures less than 53.8°C. At 80°C, the water production of TuSS was almost twice that of SSS. This occurred because, besides the different flow patterns analyzed above, the condensation surface area of TuSS was much larger than that of SSS. It should be noted that, although the h_c values of the SSS at 50°C and 80°C were approximately identical, the hourly yield of the SSS at 50°C was significantly lower than that at 80°C. This occurred because the h_c value was deduced from the temperature gradient, as shown in Eq. (7), while water production was derived from the vapor mass fraction gradient, as shown in Eq. (8). The temperature gradient was roughly identical due to the fixed temperature difference ($T_w - T_g$), as shown in Fig. 15. Meanwhile, the mass fraction gradient varied

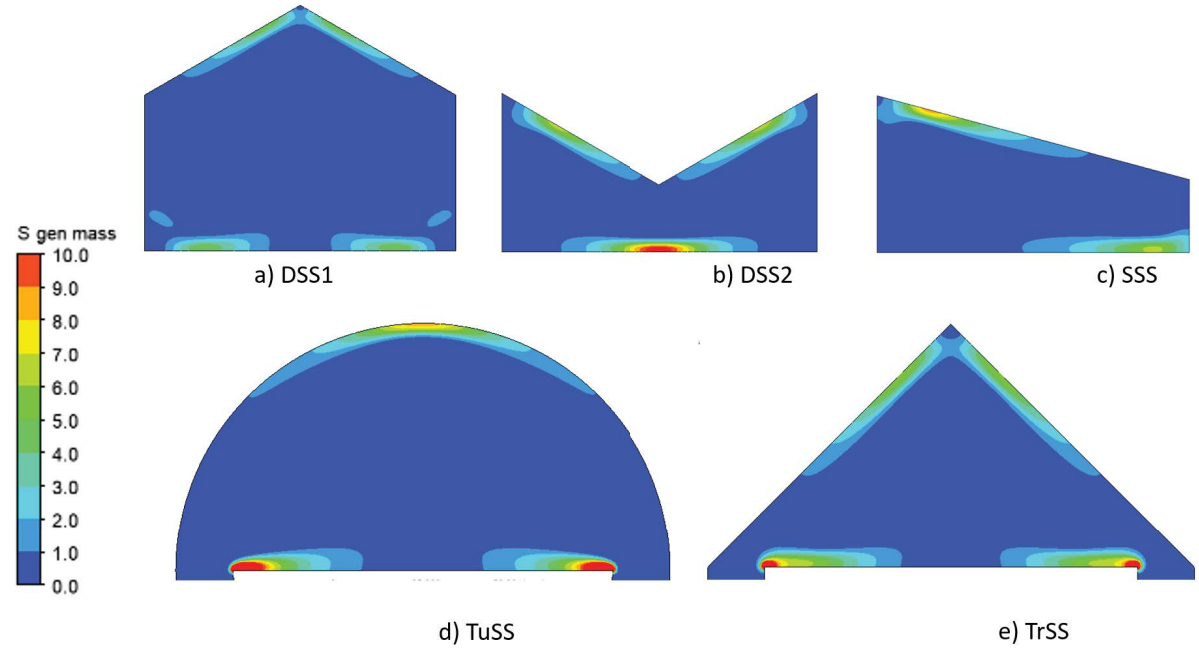

Fig. 10. Entropy generation caused by mass transfer (W/m^3·K) inside the solar stills at T_w = 60°C. (a) DSS1, (b) DSS2, (c) SSS, (d) TuSS and (e) TrSS.

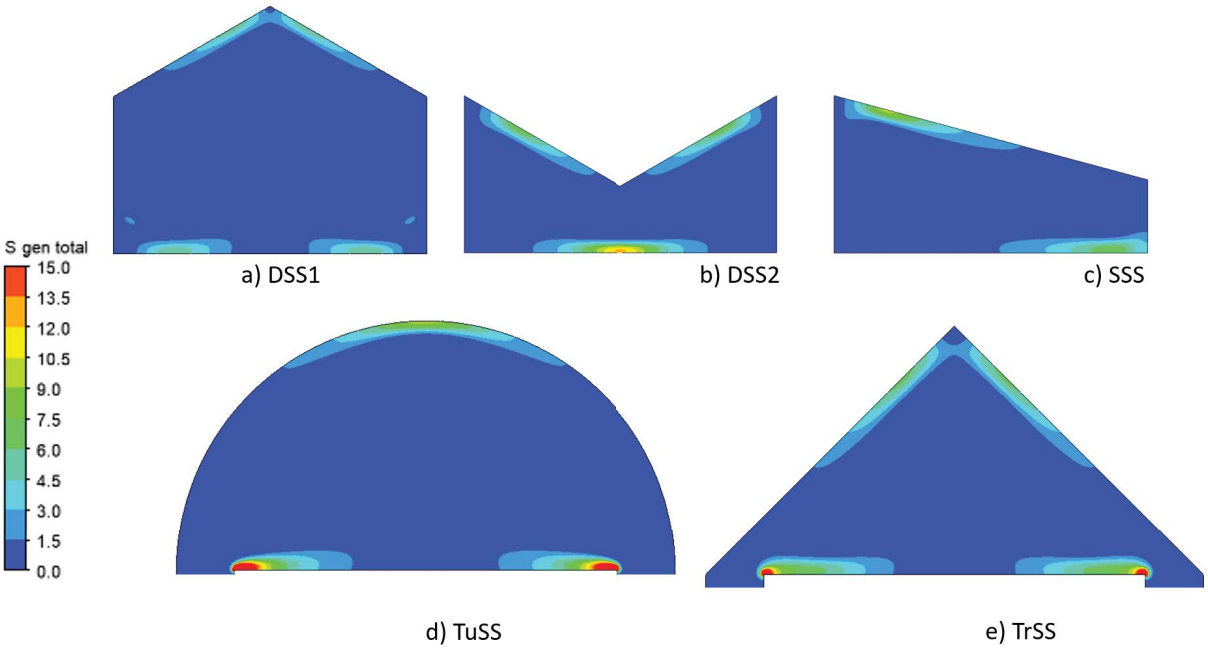

Fig. 11. Total local volumetric entropy generation (W/m^3·K) inside the solar stills at T_w = 60°C. (a) DSS1, (b) DSS2, (c) SSS, (d) TuSS and (e) TrSS.

considerably at different water temperatures, as shown in Fig. 16. As the water temperature decreased, the difference in the mass fraction of the water surface and the cover decreased sharply, as shown in Fig. 17. The mass fraction difference was the driving force behind the mass transfer. Therefore, the freshwater productivity of SSS at 80°C is three times greater than that at 50°C.

Figs. 8–11 show the local values of entropy generation. The average entropy generation in the enclosure is represented in Figs. 18–21. In general, entropy generation characterizes the degree of chaos in a system. Therefore, from the figures it can be observed that the three-vortex flow field of the SSS had the highest entropy generation for the same water temperature, especially the entropy generation that

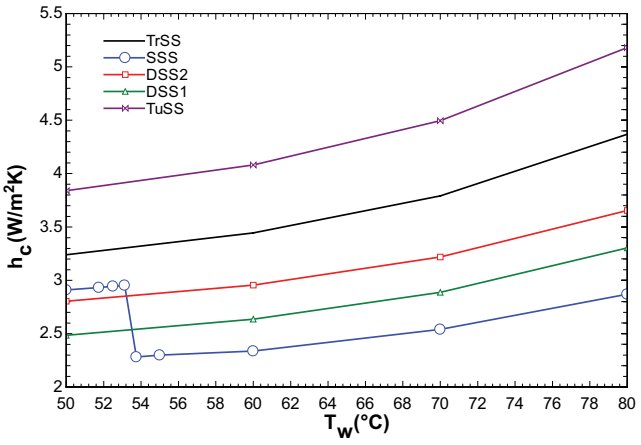

Fig. 12. Variations in the convection heat transfer coefficient based on water temperature and solar still design.

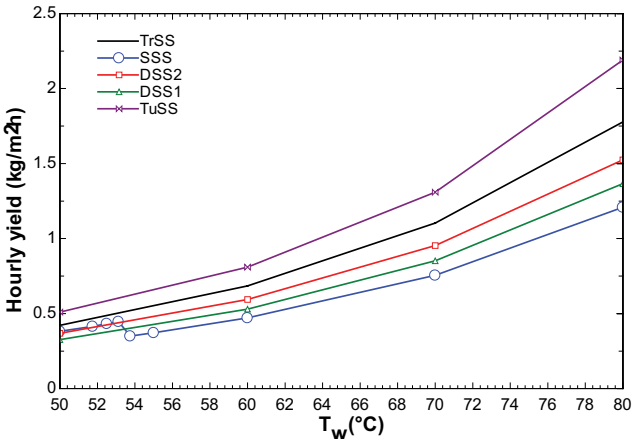

Fig. 14. Variations in water productivity based on water temperature and solar still design.

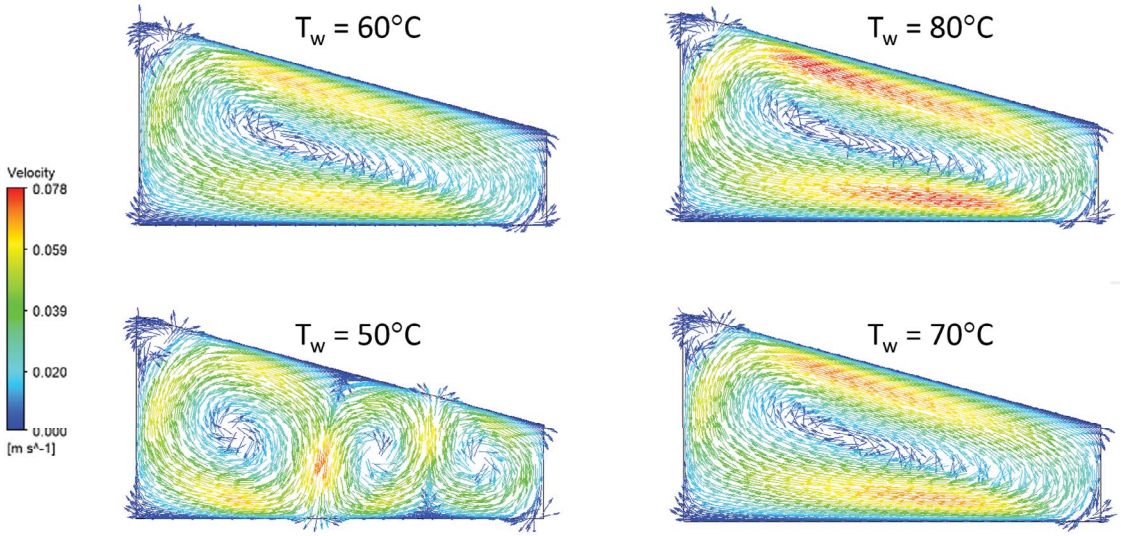

Fig. 13. Velocity vector of the single-slope still (SSS) at various water temperatures.

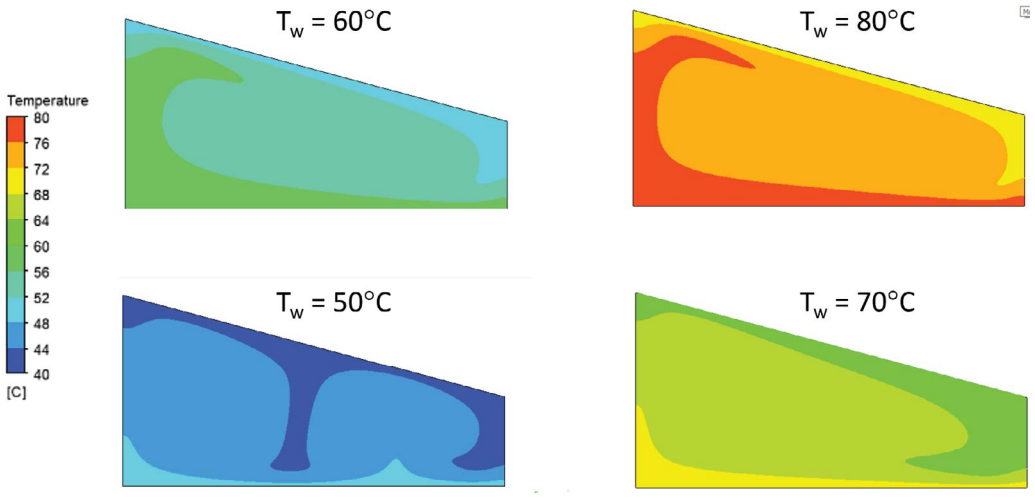

Fig. 15. Temperature field of the single-slope still (SSS) at various water temperatures.

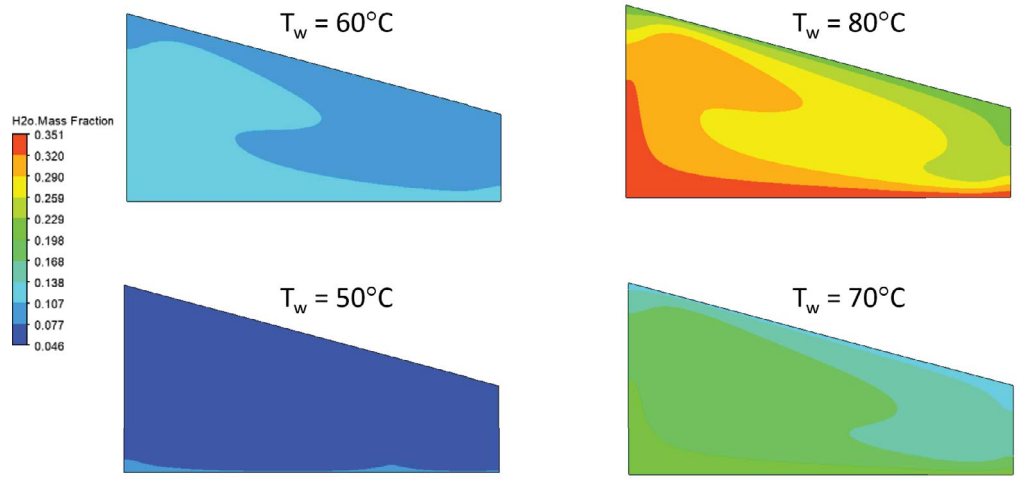

Fig. 16. Water vapor mass fraction distribution of the single-slope still (SSS) at various water temperatures.

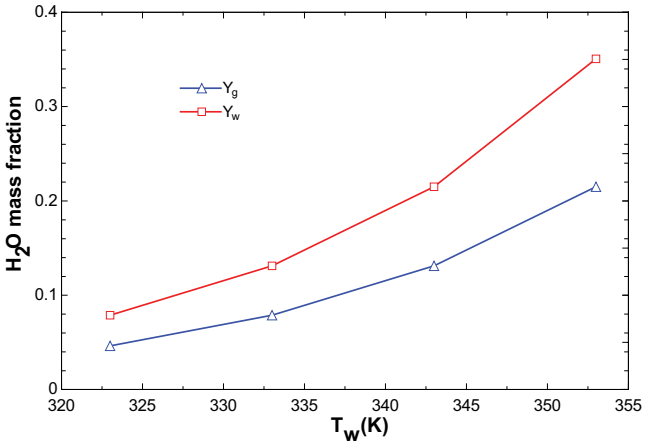

Fig. 17. Water vapor mass fraction at water surface (Y_w) and glass cover (Y_g) at various water temperatures.

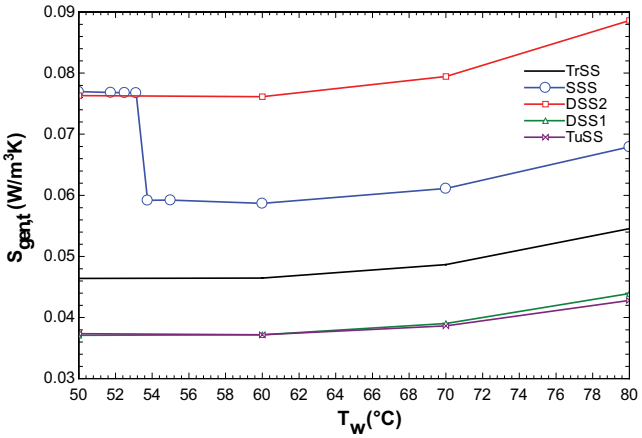

Fig. 19. Thermal entropy generation based on water temperature and solar still design.

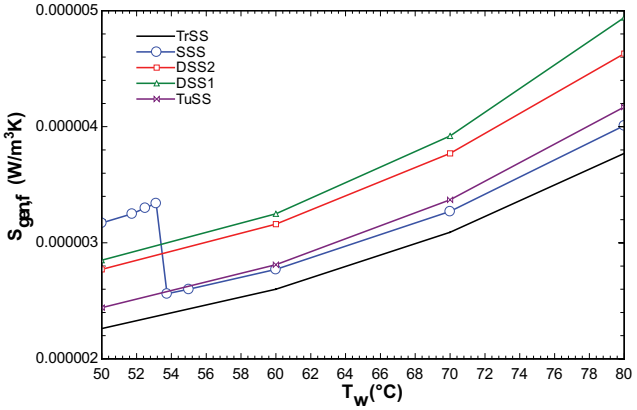

Fig. 18. Frictional entropy generation based on water temperature and solar still design.

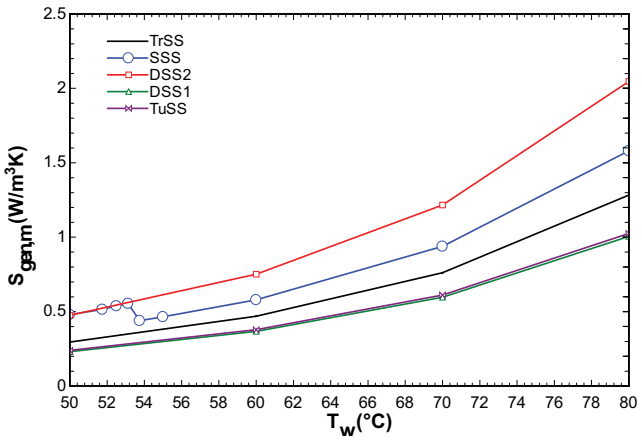

Fig. 20. Diffusive entropy generation based on water temperature and solar still design.

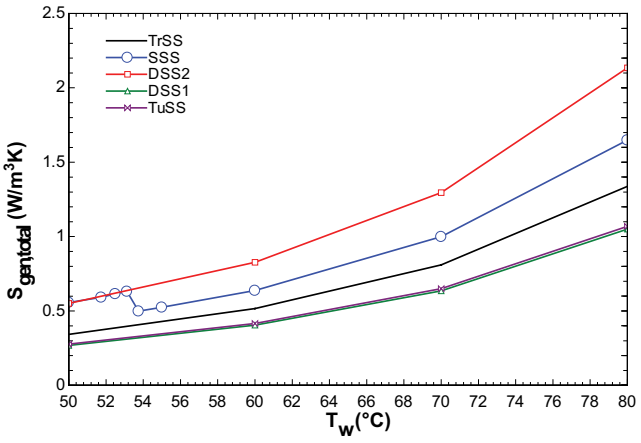

Fig. 21. Total entropy generation based on water temperature and solar still design.

was due to friction. At water temperatures greater than 53°C, the entropy generation of DSS2 was the greatest. This was due to the disorder of the impinging jet moving downward and the steam rising upward. The perturbation increased the entropy generation due to the heat transfer and diffusion of DSS2. The entropy generations of DSS1 and TuSS were the lowest and almost identical. Based on the heat and fluid flow fields and sensitivity analyses, it was concluded that the transport phenomena in the distillation enclosure were governed by the variations in the vapor concentrations based on temperature, and CFD was a suitable tool for the performance prediction and explanation of simultaneous transfer characteristics in the enclosure rather than in the experimental method.

4. Conclusions

In this study, two-dimensional simulations of five solar stills were performed. The solar stills had an identical water surface area in order to compare their water yield rate and entropy generation. The important results drawn from this study were as follows:

- DSS2 had the highest entropy generation; however, DSS2 possessed greater productivity compared to DSS1 and SSS. At a water temperature of 80°C, the freshwater productions of DSS2, DSS1, and SSS were 1.53, 1.37, and 1.21 kg/m^2·h, respectively.
- For SSS, a primary vortex was created when the water temperature was greater than 53°C. At this temperature or lower, three vortices formed inside the distillation chamber of the SSS. The performance rate increased during the transition from one rotation region to three.
- The TuSS had the highest water productivity and the lowest entropy generation. At operating temperatures above 53°C, its production rate was twice as high as that of the SSS.
- The TrSS had the second highest water production, and its entropy generation was less than that of the SSS. At a water temperature of 80°C, the entropy generations of TrSS and SSS were 1.34 and 1.65 W/m^3·K, respectively.
- The impingement jet on the water surface of DSS2 increased the entropy generation due to heat and mass transfer.
- Large rotation zones on two sides of the DSS1's water surface reduced freshwater production.
- In general, the water production and total entropy generation of the stills were as follows:

	Water production	Total entropy generation
T_w < 53°C	DSS1 < SSS = DSS2 < TrSS < TuSS	TuSS = DSS1 < TrSS < SSS = DSS2
T_w > 53°C	SSS < DSS1 < DSS2 < TrSS < TuSS	TuSS = DSS1 < TrSS < SSS < DSS2

The potential future scope of the conducted research is a transient simulation. Additionally, consideration of the liquid phase of salty water, the solid phase of glass covers, and thermal insulation were not included in this study.

Acknowledgments

This research is funded by the Industrial University of Ho Chi Minh City (IUH) under grant number 22/2NL01.

Symbols

D_m	—	Mass diffusivity of vapor, m^2/s
g	—	Acceleration of gravity, m/s^2
h_c	—	Convective heat transfer coefficient, W/m^2·K
k	—	Thermal conductivity, W/m·K
L	—	Length of water surface, m
$\dot{m}$	—	Hourly water productivity, kg/m^2·h
n	—	Normal direction
p	—	Pressure, Pa
R	—	Ideal gas constant, J/kg·K
$S_{gen,f}$	—	Volumetric entropy generation due to friction, W/m^3·K
$S_{gen,m}$	—	Volumetric entropy generation due to mass transfer, W/m^3·K
$S_{gen,t}$	—	Volumetric entropy generation due to heat transfer, W/m^3·K
T	—	Temperature, °C
u	—	x-component of velocity, m/s
v	—	y-component of velocity, m/s
x	—	x-direction in Cartesian coordinate
Y	—	Water vapor mass fraction
y	—	y-direction in Cartesian coordinate

Greek

α	—	Thermal diffusivity, m^2/s
β	—	Volume expansion coefficient, K^{-1}
β_s	—	Species expansion coefficient, m^3/kg
μ	—	Dynamic viscosity, kg/m·s
ν	—	Kinematic viscosity, m^2/s
ρ	—	Density, kg/m^3

φ — Relative humidity

Subscripts

g — Glass cover
o — Operating condition
w — Water surface

Abbreviations

DSS1 — Double-slope solar still type 1 (greenhouse-type solar still)
DSS2 — Double-slope solar still type 2 (V-type solar still)
SSS — Single-slope still
TrSS — Triangular solar still
TuSS — Tubular solar still

References

[1] Y. Sarray, N. Hidouri, A. Mchirgui, A.B. Brahim, Study of heat and mass transfer phenomena and entropy rate of humid air inside a passive solar still, Desalination, 409 (2017) 80–95.
[2] K.Q. Vo, C.H. Le, A.Q. Hoang, Optimization of mass flow rate ratio of water and air in humidification–dehumidification desalination systems, Desal. Water Treat., 246 (2022) 82–91.
[3] A. Rahmani, A. Boutriaa, Numerical and experimental study of a passive solar still integrated with an external condenser, Int. J. Hydrogen Energy, 42 (2017) 29047–29055.
[4] M. Edalatpour, K. Aryana, A. Kianifar, G. Tiwari, O. Mahian, S. Wongwises, Solar stills: a review of the latest developments in numerical simulations, Sol. Energy, 135 (2016) 897–922.
[5] K. Voropoulos, E. Mathioulakis, V. Belessiotis, Transport phenomena and dynamic modeling in greenhouse-type solar stills, Desalination, 129 (2000) 273–281.
[6] B.S. Kumar, S. Kumar, R. Jayaprakash, Performance analysis of a "V" type solar still using a charcoal absorber and a boosting mirror, Desalination, 229 (2008) 217–230.
[7] P. Suneesh, R. Jayaprakash, T. Arunkumar, D. Denkenberger, Effect of air flow on "V" type solar still with cotton gauze cooling, Desalination, 337 (2014) 1–5.
[8] D. Purnachandrakumar, G. Mittal, R.K. Sharma, D.B. Singh, S. Tiwari, H. Sinhmar, Review on performance assessment of solar stills using computational fluid dynamics (CFD), Environ. Sci. Pollut. Res., 29 (2022) 38673–38714.
[9] S.S. AlSaleem, E. Al-Qadami, H.Z. Korany, Md. Shafiquzzaman, H. Haider, A. Ahsan, M. Alresheedi, A. AlGhafis, A. AlHarbi, Computational fluid dynamic applications for solar stills efficiency assessment: a review, Sustainability, 14 (2022) 10700, doi: 10.3390/su141710700.
[10] N. Rahbar, A. Asadi, E. Fotouhi-Bafghi, Performance evaluation of two solar stills of different geometries: tubular versus triangular: experimental study, numerical simulation, and second law analysis, Desalination, 443 (2018) 44–55.
[11] M. Keshtkar, M. Eslami, K. Jafarpur, A novel procedure for transient CFD modeling of basin solar stills: coupling of species and energy equations, Desalination, 481 (2020) 114350, doi: 10.1016/j.desal.2020.114350.
[12] M. Keshtkar, M. Eslami, K. Jafarpur, Effect of design parameters on performance of passive basin solar stills considering instantaneous ambient conditions: a transient CFD modeling, Sol. Energy, 201 (2020) 884–907.
[13] S. Ashtiani, F. Hormozi, Design improvement in a stepped solar still based on entropy generation minimization, J. Therm. Anal. Calorim., 140 (2020) 1095–1106.
[14] N. Rahbar, J.A. Esfahani, Productivity estimation of a single-slope solar still: theoretical and numerical analysis, Energy, 49 (2013) 289–297.
[15] S. Shoeibi, H. Kargarsharifabad, N. Rahbar, G. Ahmadi, M.R. Safaei, Performance evaluation of a solar still using hybrid nanofluid glass cooling-CFD simulation and environmental analysis, Sustainable Energy Technol. Assess., 49 (2022) 101728, doi: 10.1016/j.seta.2021.101728.
[16] M. Edalatpour, A. Kianifar, S. Ghiami, Effect of blade installation on heat transfer and fluid flow within a single slope solar still, Int. Commun. Heat Mass Transfer, 66 (2015) 63–70.
[17] S. Rashidi, S. Akar, M. Bovand, R. Ellahi, Volume of fluid model to simulate the nanofluid flow and entropy generation in a single slope solar still, Renewable Energy, 115 (2018) 400–410.
[18] N. Rahbar, J.A. Esfahani, E. Fotouhi-Bafghi, Estimation of convective heat transfer coefficient and water-productivity in a tubular solar still–CFD simulation and theoretical analysis, Sol. Energy, 113 (2015) 313–323.
[19] S.W. Sharshir, Y.M. Ellakany, A.M. Algazzar, A.H. Elsheikh, M.R. Elkadeem, E.M.A. Edreis, A.S. Waly, R. Sathyamurthy, H. Panchal, M.S. Elashry, A mini review of techniques used to improve the tubular solar still performance for solar water desalination, Process Saf. Environ. Prot., 124 (2019) 204–212.
[20] S. Subhani, R.S. Kumar, Numerical performance evaluation of tubular solar still with different geometries of water basin, Desal. Water Treat., 196 (2020) 360–369.
[21] T. Yan, G. Xie, H. Liu, Z. Wu, L. Sun, CFD investigation of vapor transportation in a tubular solar still operating under vacuum, Int. J. Heat Mass Transfer, 156 (2020) 119917, doi: 10.1016/j.ijheatmasstransfer.2020.119917.
[22] S. Chen, P. Zhao, G. Xie, Y. Wei, Y. Lyu, Y. Zhang, T. Yan, T. Zhang, A floating solar still inspired by continuous root water intake, Desalination, 512 (2021) 115133, doi: 10.1016/j.desal.2021.115133.
[23] G. Mittal, An unsteady CFD modelling of a single slope solar still, Mater. Today Proc., 46 (2021) 10991–10995.
[24] S. Rashidi, J.A. Esfahani, Spatial entropy generation analysis for the design improvement of a single slope solar still, Environ. Prog. Sustainable Energy, 37 (2018) 1112–1120.
[25] S. Rashidi, L. Yang, A. Khoosh-Ahang, D. Jing, O. Mahian, Entropy generation analysis of different solar thermal systems, Environ. Sci. Pollut. Res., 27 (2020) 20699–20724.